Constraints on the dust extinction law of the Galaxy with Swift /UVOT, Gaia , and 2MASS

Ignacio Ferreras, Mónica Tress, Gustavo Bruzual, Stéphane Charlot, Mat Page, Vladimir Yershov, Paul Kuin, Daisuke Kawata, Mark Cropper

Monthly Notices of the ROYAL ASTRONOMICAL SOCIETY

MNRAS **505,** 283–292 (2021) doi:10.1093/mnras/stab1270
Advance Access publication 2021 May 6

Constraints on the dust extinction law of the Galaxy with *Swift*/UVOT, *Gaia*, and *2MASS*

Ignacio Ferreras [1,2,3,4]★ Mónica Tress,[2] Gustavo Bruzual,[5] Stéphane Charlot,[6] Mat Page,[2] Vladimir Yershov,[2] Paul Kuin,[2] Daisuke Kawata [2] and Mark Cropper[2]

[1]*Instituto de Astrofísica de Canarias, Calle Vía Láctea s/n, E-38205 La Laguna, Tenerife, Spain*
[2]*Mullard Space Science Laboratory, University College London, Holmbury St Mary, Dorking, Surrey RH5 6NT, UK*
[3]*Department of Physics and Astronomy, University College London, London WC1E 6BT, UK*
[4]*Departamento de Astrofísica, Universidad de La Laguna, E-38206 La Laguna, Tenerife, Spain*
[5]*Instituto de Radioastronomía y Astrofísica, UNAM, Campus Morelia, Michoacán, México CP 58089, México*
[6]*Sorbonne Université, CNRS, UMR7095, Institut d'Astrophysique de Paris, F-75014 Paris, France*

Accepted 2021 April 30. Received 2021 April 30; in original form 2020 November 17

ABSTRACT

We explore variations of the dust extinction law of the Milky Way by selecting stars from the *Swift*/UVOT Serendipitous Source Catalogue, cross-matched with *Gaia* DR2 and *2MASS* to produce a sample of 10 452 stars out to ∼4 kpc with photometry covering a wide spectral window. The near ultraviolet passbands optimally encompass the 2175 Å bump, so that we can simultaneously fit the net extinction, quoted in the V band (A_V), the steepness of the wavelength dependence (δ), and the bump strength (E_b). The methodology compares the observed magnitudes with theoretical stellar atmospheres from the models of Coelho. Significant correlations are found between these parameters, related to variations in dust composition that are complementary to similar scaling relations found in the more complex dust attenuation law of galaxies – that also depend on the distribution of dust among the stellar populations within the galaxy. We recover the strong anticorrelation between A_V and Galactic latitude, as well as a weaker bump strength at higher extinction. δ is also found to correlate with latitude, with steeper laws towards the Galactic plane. Our results suggest that variations in the attenuation law of galaxies cannot be fully explained by dust geometry.

Key words: dust, extinction – ISM: general – Galaxy: general.

1 INTRODUCTION

Dust is one of the key observable components of galaxies. Through absorption and scattering, dust affects the way starlight reaches the observer, and a good characterization of the wavelength dependence of these processes is fundamental to be able to, for instance, derive accurate stellar masses or star formation rates of galaxies. There are two main ways in which the presence of dust will shape the spectral energy distribution of a galaxy: the dust properties will lead to an extinction law that reflects how the superposition of dust grains of different size and composition absorbs and scatters incoming light (see e.g. Draine 2003). In addition, the distribution of dust within the galaxy will affect light from the constituent stellar populations in different ways. Most importantly, light from other regions of the galaxy may be scattered *into* the line of sight to the observer, complicating the interpretation of attenuation, that no longer depends exclusively on dust composition (see e.g. Witt & Gordon 2000; Panuzzo et al. 2007). A deeper understanding of the dust extinction law in the Milky Way Galaxy and its variations will help remove these degeneracies. Note studies of dust extinction in the Milky Way are free from such effects, as we are simply probing direct lines of sight to stars. We emphasize that extinction and attenuation are different concepts measured in similar ways. For instance, clumpiness in the distribution of dust, typically found in star forming regions, will affect the steepness of the wavelength dependence of the attenuation law (e.g. Witt & Gordon 2000), whereas the same steepness parameter only depends on dust composition when considering extinction, as it is measured along a single line of sight towards a star (e.g. Fitzpatrick & Massa 1990). This paper focuses solely on dust extinction as we are observing single stars in our Galaxy. Therefore, any variations found in the derived parameters can only be caused by changes in dust composition.

The observations in the Milky Way and the Magellanic Clouds reveal an overarching trend towards higher extinction at shorter wavelengths, along with a reduced set of spectral features, most notably the 2175 Å NUV bump and the 9.7 μm and 18 μm silicate features (see e.g. Galliano, Galametz & Jones 2018). The most likely candidate to explain the NUV bump – targeted in this paper – is related to the resonance present in benzene-based structures such as polycyclic aromatic hydrocarbons (PAHs; see e.g. Duley & Seahra 1998). However there are other potential carriers (Bradley et al. 2005), so a full account of this feature remains an open question. There has been a number of parameterizations of the wavelength dependence of the extinction law in the Milky Way, and the observational constraints led to the definition of standard extinction laws, although with a large amount of scatter among different sightlines (see e.g. Cardelli, Clayton & Mathis 1989;

★ E-mail: iferreras@iac.es

Fitzpatrick & Massa 1990; Fitzpatrick 1999). The extinction law of the Small Magellanic Cloud (SMC; Pei 1992; Gordon et al. 2003) features a steeper wavelength dependence, characteristic of smaller dust grains (see e.g. Weingartner & Draine 2001). In addition, the SMC law also lacks the NUV bump (Hagen et al. 2017). Knowledge of the dependence of the scatter of the extinction law on dust composition allows us to extend the analysis to dust attenuation in unresolved galaxies to find out about dust composition (see e.g. Tress et al. 2019)

The UVOT camera (Roming et al. 2005) on board the *Neil Gehrels Swift Observatory* features three NUV filters, UVW2, UVM2, and UVW1, that straddle the 2175 Å bump, along with three standard *U*, *B*, *V* filters in the optical spectral window. The optimal location of the NUV passbands has been exploited in studies to constrain the dust attenuation law in nearby galaxies (e.g. Hoversten et al. 2011; Hutton et al. 2014; Decleir et al. 2019) as well as the dust extinction law in the SMC (Hagen et al. 2017). For instance, in Hutton et al. (2014) it was shown that the attenuation law in nearby prototypical starburst galaxy M82 cannot be explained by the standard starburst prescription of Calzetti et al. (2000), as the NUV bump is present throughout the galaxy. Moreover, a substantial radial gradient was evident in the strength of the bump and the total-to-selective extinction parameter, R_V (Hutton, Ferreras & Yershov 2015).

This paper explores a large archival sample of stars observed by the UVOT camera, cross-matched with the *Gaia* and *2MASS* catalogues, as presented in Section 2. The methodology that allows us to extract constraints on the dust extinction parameters is presented in Section 3, including an analysis based on simulated data to explore the systematics. A discussion of the results is shown in Section 4, followed by a summary in Section 5. Throughout this paper, all magnitudes are quoted in the AB system (Oke & Gunn 1983).

2 DATA

This work focuses on photometric data from the UVOT Serendipitous Source catalogue (UVOT/SSC; Page et al. 2014; Yershov et al. 2014), a compilation of all sources (resolved and unresolved) found in the archive of observations taken by the *Swift*/UVOT instrument, produced by processing all archival data. We use v1.1 of the UVOT/SSC catalogue, comprising a total of 23 059 observations in which over 13.86 million sources are detected, although we note that the same sources could have been observed repeatedly in several runs. The number of unique sources in this catalogue, with available fluxes in all six photometric bands is 170 801. From this set, we select those observations with good photometric measurements – defined as those with an uncertainty below 0.2 mag in all six passbands, along with a quality flag equal to zero. This constraint ensures good accuracy in the derivation of the dust extinction parameters, as we show below, and only decreases the sample size by 8.8 per cent. The sample is cross-matched with the *Gaia* DR2 (Gaia Collaboration 2018) stellar catalogue, selecting those sources with an available effective temperature from Bai et al. (2019), and a distance estimate from Bailer-Jones et al. (2018). The set is also matched with the point source catalogue of *2MASS* (Cutri et al. 2003) to include NIR photometry in the *J*, *H*, and K_s passbands. The cross-matching was done with the help of the excellent service provided by the Centre de Données astronomiques de Strasbourg (CDS).[1] The sample from this cross-match comprises 80 104 stars. Fig. 1 shows the response of the nine passbands used in this study – separated into the UVOT NUV and optical filters, (left) and the 2MASS NIR filters (right). For reference, the standard dust extinction law of the Milky Way is shown (Cardelli et al. 1989).

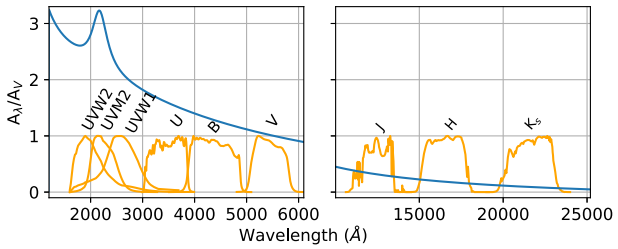

Figure 1. The standard extinction law usually adopted for the Milky Way (corresponding to $E_b = 4$ and $\delta = -0.05$) is shown, along with the normalized response of the passbands used in the analysis.

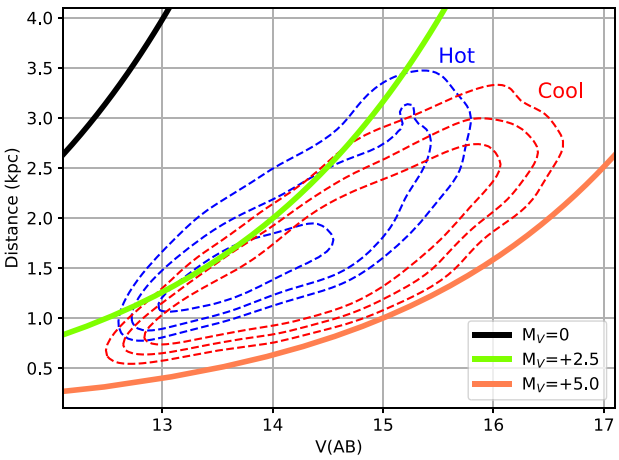

Figure 2. Distribution of stars on the distance versus *V*-band apparent magnitude plane. The contours trace the density of stars of our working sample on this diagram, split with respect to effective temperature at the median value ($T_{\rm eff} = 7500$ K). From the inside out, the contours encompass 90, 95, and 99 per cent of the hot/cool subsets. For reference, the black, green, and orange lines represent the expected loci of an unreddened star with absolute *V*-band magnitude of 0, +2.5, and +5, respectively.

One of the key parameters explored in this paper is the 2175 Å bump, that requires a significant amount of flux in the NUV bands. Trial and error in our methodology (see below) results in setting a lower limit in the effective temperature to be able to constrain the dust extinction parameters. We opted to impose a threshold in the effective temperature, $T_{\rm eff} > 6500$ K, producing a final working sample that comprises 10 452 stars. We emphasize that the temperature mentioned here has been obtained independently, using a supervised machine learning algorithm (Bai et al. 2019), trained on a standard assumption for the dust extinction law. Since we adopt a more generic function, the actual values of the temperature may vary. However, we only use this one to impose a Gaussian prior in the analysis, as shown in the next section. Hence, the final estimates of temperature will be consistent with the best-fitting extinction law for each star.

The distribution of the sample in the distance versus apparent magnitude plane is shown in Fig. 2, split at the median $T_{\rm eff}$ (7500 K) with hot and cold stars shown as blue/red dashed contours, respectively. From the inside out, the contours engulf 90, 95, and 99 per cent of each subset. We note that due to both sample selection and the actual distribution of stars as a function of temperature, the cooler subsample mostly consists of A- and F-type stars. For

[1] http://cdsxmatch.u-strasbg.fr

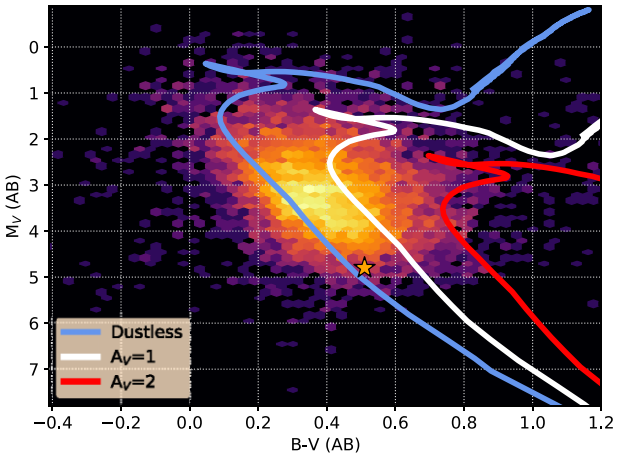

Figure 3. Distribution of the sample on the absolute V band magnitude versus $B-V$ plane. The conversion from apparent to absolute magnitude makes use of the *Gaia* DR2 distances. For reference, a solar metallicity isochrone at 1 Gyr of age (from the PARSEC team, Bressan et al. 2012; see e.g. Alzate, Bruzual & Díaz-González 2021) is shown in the dustless case (blue), or introducing a V band extinction of $A_V = 1$ (white) or 2 mag (red) for a Milky Way standard dust law (Cardelli et al. 1989). The location of the Sun is shown in this diagram as a star for reference.

reference, the figure includes the expected location of unreddened stars with absolute V-band magnitude of 0, +2.5, and +5.0 (black, green, and orange lines, respectively). The number of stars drops at apparent magnitudes fainter than $V \gtrsim 16.5$ AB, and extends to a distance $\lesssim$4 kpc. It is also worth noting that a segregation based on colour does not introduce a bias regarding distance or apparent magnitude. This will be relevant when we explore in Section 4 the distribution of dust extinction parameters.

Fig. 3 shows the sample in a Hertzsprung–Russell diagram, with V-band absolute magnitude against $B-V$ colour. For reference, a solar metallicity, 1 Gyr isochrone from the PARSEC team (Bressan et al. 2012) is overlaid, including the effect of extinction, as labelled, adopting a standard Milky Way extinction law ($R_V = 3.1$; see e.g. Cardelli et al. 1989). Models based on these isochrones provide accurate fits to the observed colour–magnitude distribution of the *Gaia* data (Alzate et al. 2021). This choice is only meant to illustrate the location of our data on a standard colour–magnitude diagram. As the population ages, the main sequence turnoff will shift towards redder and fainter values, in the same direction as an increased dust extinction, reflecting the well-known age-dust degeneracy of stellar populations. This work does not attempt to fit isochrones, and focuses instead on a combined constraint of the temperature and dust extinction from the observed fluxes of single stars. This figure illustrates the nature of our sample as mostly turn-off and sub-giant stars with a range of extinction $A_V \lesssim 2$ mag. Our sample is biased in favour of the brighter and bluer sources, as we impose detection in all NUV and optical filters from the UVOT catalogue as the main selection criterion. This implies a preponderance of stars on the Galactic plane (90 per cent of the sample has Galactic latitude $b \lesssim 20^\circ$), and allows us to cover a wide range of distance, with 90 per cent of the sample probing out to $\lesssim$ 3.3 kpc, without a significant bias regarding temperature (Fig. 2).

3 METHODOLOGY

There are several functional forms in the literature to describe the wavelength dependence of dust extinction and attenuation (see e.g. Cardelli, Clayton & Mathis 1989; Fitzpatrick & Massa 1990, 2007; Noll et al. 2009; Conroy, Schiminovich & Blanton 2010). We choose the parametric function presented by Kriek & Conroy (2013) from the previous work of Noll et al. (2009).[2] At each wavelength, λ, the extinction, in magnitudes, can be written

$$A(\lambda) = \frac{A_V}{4.05}\left[k'(\lambda) + E_b D(\lambda)\right]\left(\frac{\lambda}{\lambda_V}\right)^{\delta}, \quad (1)$$

where $k'(\lambda)$ is the standard reddening curve found in equation (4) of Calzetti et al. (2000). The NUV bump is described by a Lorentzian-like profile, $D(\lambda)$ (often termed a Drude profile), scaled by the NUV bump strength parameter, E_b, with two additional parameters, the central wavelength, and the width. We follow Kriek & Conroy (2013) to define this absorption feature, namely adopting 2175 Å for the central wavelength and 350 Å for the width. The central wavelength does not vary among different lines of sight, but the width does show significant scatter (see e.g. Valencic, Clayton & Gordon 2004; Fitzpatrick & Massa 2007). However, it is beyond the scope of this paper to treat the width as a free parameter, so that our constraints of E_b should be taken as the effective bump strength for a fixed absorption profile. Finally, δ is a parameter that changes the steepness of the original wavelength dependence of the Calzetti et al. (2000) law – that corresponds to $E_b = 0$, $\delta = 0$. Positive/negative values of δ correspond to a shallower/steeper wavelength dependence, respectively. Note that the number 4.05 in equation (1) refers to the original total to selective extinction parameter R_V for the Calzetti law. Therefore, the wavelength dependence of this prescription is concisely defined by three parameters: A_V, E_b, and δ. An alternative description of the extinction/attenuation law is the one defined by Conroy et al. (2010), where the steepness of the law is parameterized by the more traditional R_V, and the bump strength is described by B, so that the choice $R_V = 3.1$, $B = 1$ closely follows the standard Milky Way law of Cardelli et al. (1989). In the appendix of Tress et al. (2018) a simple analytic expression is presented to convert between these two parameterizations. For instance, the Milky Way standard corresponds to $\delta \simeq -0.05$, $E_b \simeq 4$. We emphasize that our analysis, based on broadband photometry, does not consider independent variations in the wavelength dependence in the NUV and optical windows, a task that can only be attempted by use of spectroscopic data (e.g. Fitzpatrick & Massa 1990; Gordon, Cartledge & Clayton 2009; Fitzpatrick et al. 2019).

Our methodology rests on a comparison between the combined NUV, optical, and NIR photometry with a set of stellar atmospheres from the models of Coelho (2014). The spectra are retrieved in FITS format from Coelho's webpage.[3] These models include a homogeneous computation of opacity distribution functions, and provide a set of stellar spectra for a wide range of effective temperature, surface gravity, and chemical composition, including non-solar abundance ratios. However, since our analysis is based on low spectral resolution photometry using traditional broadband filters, we restrict the parameter space to effective temperature and metallicity, keeping a fixed value of surface gravity and abundance ratios. We adopt these models as they have been thoroughly tested in population synthesis models by Coelho, Bruzual & Charlot (2020), where it is shown that some of the existing discrepancies in the output of synthetic populations based on either empirical or theoretical stellar libraries is mostly due to the sampling of the underlying stellar

[2]There is no evident advantage of using this parametrization with respect to other choices, but we find this one is used rather extensively in the literature.
[3]http://www.astro.iag.usp.br/~pcoelho/

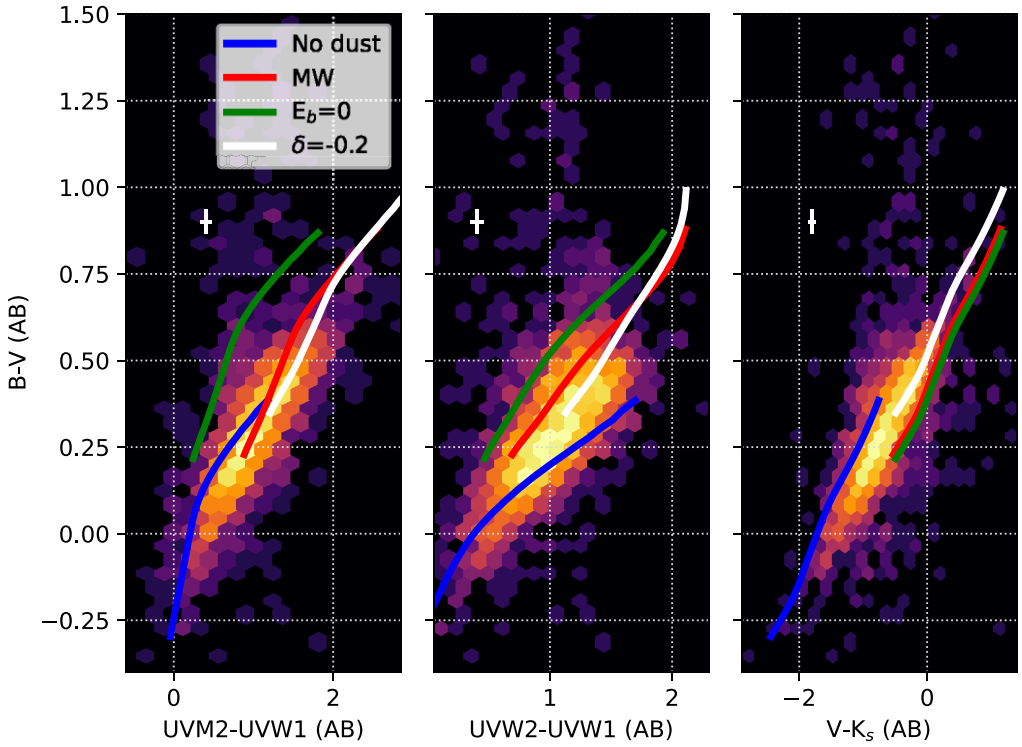

Figure 4. Colour–colour diagrams of the sample. The panels show the optical $B-V$ plotted against two NUV colours from UVOT and an optical−NIR colour ($V-K_s$). The blue lines are tracks from the stellar library used in this paper, at solar metallicity over a range of effective temperatures (6500–18 000 K), without any dust correction applied. The red lines show the effect of a Milky Way standard dust correction ($E_b=4$, $\delta=-0.05$), at $A_V=2$, and the green lines are the equivalent case, with the NUV bump set to zero ($E_b=0$, $\delta=-0.05$). The white lines adopt a change in the steepness of the extinction law, towards a stronger wavelength dependence ($\delta=-0.2$ corresponds to $R_V\sim2.6$, keeping the original bump strength $E_b=4$). A 1σ error bar in each panel illustrates the worst case scenario for the statistical uncertainty of the colour estimates.

parameters, rather than the stellar spectra themselves. Therefore, spectra from state-of-the-art stellar atmosphere models are suitable for this type of analysis and free from the dust correction residuals present in empirical data. Moreover, the computed colours based on filters with broad bandpasses only carry systematic uncertainties that are substantially smaller than the typical statistical uncertainties of the observations. We emphasize here the need to use theoretical libraries, and note that some of the stars in empirical libraries that cover NUV wavelengths, such as NGSL (Gregg et al. 2006) do suffer from a prominent absorption feature at the position of the NUV bump. This absorption is caused by dust along the line of sight to the star that would require an accurate knowledge of the properties of dust in the Milky Way along specific directions. Therefore, the model predictions from empirical spectra will be compromised.

To illustrate the power of a photometric analysis to constrain the dust extinction law, we show in Fig. 4 three colour–colour diagrams with our sample represented as a density plot. Three tracks are overlaid that correspond to models, at solar metallicity, solar abundance ratios, and surface gravity $\log g=4.5$ (cgs). The tracks cover the temperature range from T = 6500 K (top right corner of the three panels) to 18 000 K, and are shown at zero dust extinction (blue), for a Milky-Way standard law (i.e. $\delta=-0.05$, $E_b=4$) with $A_V=2$ mag (red), and for the same amount of extinction with a law that lacks the NUV bump (represented by $E_b=0$, keeping $\delta=-0.05$, green). The white line keeps the same bump strength as that of the Milky Way ($E_b=4$), but changes δ to a steeper value (-0.2) to show the effect of a change in the slope of the extinction law. The error bars show the worst case scenario for the statistical uncertainty of the colour measurements. Note, for instance, the lack of sensitivity to the bump strength of $V-K_s$, as expected, whereas the NUV colours show a substantial sensitivity. Although UVW2−UVW1 avoids the central part of this resonance, it does show a dependence on E_b given the rather extended width of this feature. Variations in the slope produce changes in colour that progressively decrease with wavelength. Making use of all these different sensitivities to the dust parameters, combining photometric information from NUV to NIR along with the optimal spectral range of the UVOT NUV filters, it is possible to constrain all three extinction parameters.

For each star in the cross-matched UVOT sample, we compare the observed fluxes with a range of stellar atmosphere models based on a grid of 42 values of effective temperature, from $T_{\rm eff}=4000$ K to 18 000 K and three values of metallicity: [Fe/H] $=-0.5$, 0.0, $+0.2$. We emphasize that although we do have a previous estimate of $T_{\rm eff}$ from Bai et al. (2019), the value is not consistent with a generic dust extinction law as the one adopted here. Therefore, it is expected that, due to the temperature-dust degeneracy, the effective temperature may change either to lower or higher values. Therefore, we take stellar atmosphere models with lower temperatures than the threshold of 6500 K. At the other end, we limit the highest temperature in the models to 18 000 K given the drop in the number of stars shown in the colour–colour plots at the hot end of the isochrone trails (Fig. 4). Also note that in this sample, none of the values of $T_{\rm eff}$ from the analysis

Table 1. Range of stellar and dust parameters.

Parameter	Range	Gridpoints
	Stellar parameters ($\log g = 4.5$, cgs)	
$T_{\rm eff}$	[4000, 18 000] K	42
[Fe/H]	$\{-0.5, 0, +0.2\}$	3
	Dust parameter (flat) priors[a]	
A_V	[0, 8.5]	–
E_b	[0,11]	–
δ	$[-1, +1]$	–

Note. [a]Note the parameters are explored as a continuous function with an MCMC sampler, and the stellar spectra are retrieved from a bilinear ($T_{\rm eff}$, [Fe/H]) interpolation of the model grid.

of Bai et al. (2019) reaches temperatures above 10 000 K. Moreover, the fits to the observed stars produce a temperature range markedly lower, as shown below. We seek a balance between runtime and accuracy. Given the low spectral resolution of broadband photometry, we opted to restrict the stellar parameters to a single value of surface gravity, $\log g = 4.5$ (cgs), and solar abundance ratios ($[\alpha/{\rm Fe}] = 0$). Different values of surface gravity do not vary significantly the colours based on broad-band fluxes. We emphasize that the dust parameters will only be constrained with flux ratios (i.e. colours), so that the luminosity of a given model cannot introduce any bias. For each trial, the solver chooses five parameters, namely $\{T_{\rm eff}$, [Fe/H], A_V, δ, $E_b\}$. The first two are used to interpolate a stellar spectrum from the grid, and the last three parameters allow us to attenuate the spectrum using the adopted extinction law. For each observed star, we define a standard (log-)likelihood,

$$\ln \mathcal{L} = \mathcal{A} - \frac{1}{2}\chi^2(T_{\rm eff}, [{\rm Fe/H}], A_V, \delta, E_b), \quad (2)$$

where $\mathcal{A}$ is a normalization factor. For each choice of the stellar parameters ($T_{\rm eff}$ and [Fe/H]), we extract an interpolated spectrum from the grid of Coelho (2014) models, then the dust extinction corresponding to the choice of dust parameters (A_V, δ, E_b) is applied to the spectra, and the magnitudes computed for each of the filters, using the official passbands in each case.[4] The value of the χ^2 statistic is computed by comparing observed and model magnitudes, taking the V-band flux as an anchor point, meaning that all stars are assumed to have the same V-band magnitude, so that only the colours are used to constrain the parameters. A standard MCMC sampler is applied to explore the five-dimensional parameter space, making use of the PYTHON code EMCEE (Foreman-Mackey et al. 2013). The MCMC solver comprises 100 chains, taking 2000 steps, from which we remove the first 500 to derive the probability distribution function of each parameter. The values of the parameters are quoted at the median of these distributions.

Flat priors are imposed on the dust parameters over a wide range of values (see Table 1 for details of the range allowed). To overcome the potential degeneracy between temperature and the dust parameters, we impose a Gaussian prior centered at the value of $T_{\rm eff}$ obtained by Bai et al. (2019) with a standard deviation corresponding to twice the quoted error. This way we will allow for a variable $T_{\rm eff}$, but will avoid fits that correspond to very different temperatures. Fig. 5 shows the distribution of the best-fitting parameters for the total sample. It is worth noting that only ∼1.4 per cent of the sample has V-band extinction higher than 2 mag. In the next section we explore the accuracy of the parameter retrieval using a simulated sample, and will determine whether substantial degeneracies are present.

[4]The passband response curves can be found at the following link: http://svo2.cab.inta-csic.es/theory/fps/.

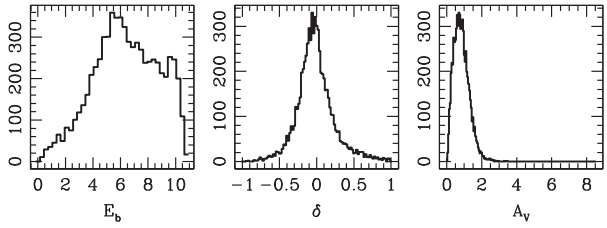

Figure 5. Distribution of the best-fitting dust extinction parameters. From left to right, the bump strength (E_b), steepness parameter (δ), and V-band extinction (A_V) are shown.

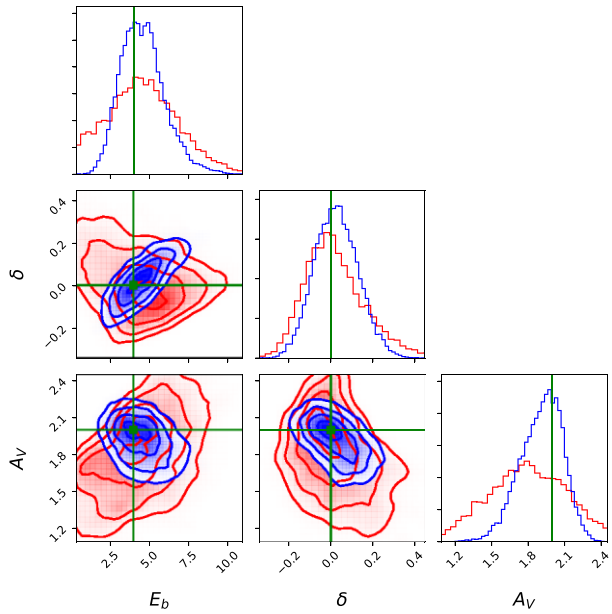

Figure 6. Retrieval of input parameters in a mock observation with 10 per cent uncertainty in the fluxes, with dust extinction parameters $E_b = 4$, $\delta = 0$, $A_V = 2$. Two stars are considered, both at solar metallicity. The four contours delimit the posterior probability at the 0.5σ, 1σ, 1.5σ, and 2σ confidence levels (from the inside out). In red we show a $T_{\rm eff} = 6500$ K star and in blue a hotter $T_{\rm eff} = 10\,000$ K star. The true values of the dust parameters are shown by the green straight lines and square symbol. The retrieved parameters are $E_b = 4.47 \pm 2.28$, $\delta = +0.01 \pm 0.15$, $A_V = 1.80 \pm 0.33$ for the cooler star and $E_b = 4.47 \pm 1.42$, $\delta = +0.02 \pm 0.10$, $A_V = 1.93 \pm 0.18$ for the hotter star (1σ uncertainties). The maximum likelihood is significantly different, with the hotter star peaking at $\mathcal{L} = 0.92$ whereas the cooler star only reaches $\mathcal{L} = 0.14$. This figure illustrates the higher accuracy at hotter effective temperatures, especially concerning the NUV bump strength.

3.1 Simulations

We test the methodology by constructing a set of mock photometric measurements, choosing a random set of dust- and stellar-related parameters, to produce the NUV, optical, and NIR fluxes. To illustrate the retrieval process for a single star, Fig. 6 shows cuts of the posterior probability distribution for two stars with the same dust extinction parameters ($E_b = 4$, $\delta = 0$ $A_V = 2$, represented by the green lines) and different effective temperatures: 6500 K (red) and 10 000 K (blue). The contours are shown at four confidence levels: 0.5σ, 1σ, 1.5σ, and 2σ. The lower temperature case produces a less accurate constraint

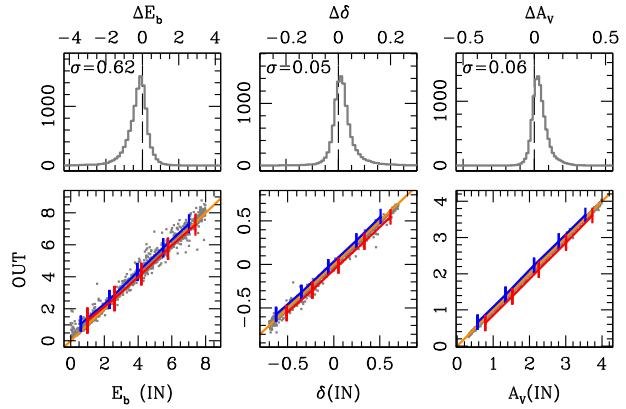

Figure 7. Retrieval of dust extinction parameters from mock observations produced from the theoretical stellar spectra subject to dust extinction obtained from a random selection of the parameters. The bottom row shows the comparison between the input parameters (horizontal) and those determined by the MCMC algorithm (vertical), with the orange line marking the ideal 1:1 correspondence. The individual measurements are shown as grey dots. The blue and red lines show the averaged results in the two subsamples – split at the median $T_{\rm eff} = 7500$ K – with the higher/lower effective temperature in blue and red, respectively. The error bars represent the 1σ scatter. The top row shows the distributions $\Delta p \equiv p_{\rm IN} - p_{\rm OUT}$, where p is one of the three dust extinction parameters (from left to right: E_b, δ, A_V). The number in each panel gives the standard deviation.

of the parameters, as expected, since cooler stars do not have enough NUV flux to probe in detail the extinction law.

Each synthetic observation has compatible photometric uncertainties with respect to the original sample: the mock set comprises the same number of stars (10 452), and for each one we use the original $T_{\rm eff}$ and flux uncertainties. In this way, we guarantee that the simulations mimick as much as possible the properties of the original sample. A random value of the metallicity (from a uniform deviate in log space, between [Fe/H] $= -0.5$ and $+0.2$) and dust parameters (also uniform deviates, $E_b \in [0, 8]$, $\delta \in [-0.7, +0.7]$, $A_V \in [0.3, 4]$) are chosen for each star, producing the fluxes according to the theoretical models adopted in this work. Note that the range is different from the grid models explored in Table 1. The grid models are expected to extend over a significantly larger range than the actual dust parameters of the sample, for robustness. Fig. 5 shows that the parameters extracted from the actual observations are contained within the intervals explored in the simulated data, thus justifying this choice. We note the distribution of E_b appears truncated at high values, but the results presented below do not show any pile up at high bump strengths in the trends, so we do not anticipate any systematic effect from the chosen range of values for E_b. The comparison between input and output are shown in Fig. 7. The bottom row compares the input parameters (horizontal axes), with respect to the ones retrieved by the MCMC-based methodology described above. Individual mock stars are shown as grey dots, and closely follow the ideal 1:1 trend (orange lines). To explore a potential systematic, we split the sample into high (blue) and low (red) effective temperature, with the cut at 7500 K (that corresponds to the median of the sample). The lines show the averaged trends, with the error bars spanning one standard deviation. No significant segregation is found within error bars, although the cooler stars consistently produce lower values of A_V and δ, with differences that are, nevertheless very small. The top row shows the distribution of the difference between input and output (grey histograms), i.e. $\Delta p \equiv p_{\rm IN} - p_{\rm OUT}$, where p is one of the three dust extinction parameters. The behaviour is acceptable,

Table 2. Pearson correlation coefficients between parameters. The values are obtained from a bootstrap that creates 200 random realizations of the data, quoting the median and the standard deviation in each case, from left to right: the input and output from simulated data, used to test the methodology (see Section 3.1), and the actual observations.

Params	Mocks		Observations
	IN	OUT	
(1)	(2)	(3)	(4)
δ versus A_V	-0.0144	$+0.0042 \pm 0.0045$	$+0.1105 \pm 0.0058$
E_b versus A_V	-0.0125	$+0.0415 \pm 0.0063$	-0.2727 ± 0.0051
δ versus E_b	-0.0065	$+0.0205 \pm 0.0065$	$+0.1032 \pm 0.0073$
A_V versus $T_{\rm eff}$	$+0.0102$	$+0.0460 \pm 0.0081$	$+0.5455 \pm 0.0054$

with standard deviations shown in the panels, namely $\Delta E_b = 0.62$; $\Delta\delta = 0.05$; $\Delta A_V = 0.06$. The 1σ uncertainties extracted from the posterior of the individual star measurements have median values $\sigma(E_b) = 1.63$; $\sigma(\delta) = 0.11$; $\sigma(A_V) = 0.25$. Although temperature is treated as a nuisance parameter, the simulations produce good results with differences between the input values and the extracted ones of $\Delta T_{\rm eff} = 37 \pm 78$ K.

We also emphasize that for each star the dust law is determined from a random set of parameters (A_V, δ, E_b), so that no spurious correlation should be expected between them. This sanity check allows us to assess whether there is any systematic from the underlying degeneracies when comparing the results with actual stars. Columns 2 and 3 of Table 2 show the Pearson correlation coefficients of the input and output parameters for four pairings. The data for the output includes the 1σ scatter derived from bootstrapping according to the retrieved error in each parameter. Most importantly, only a weak covariance is found between A_V and both bump strength and effective temperature, and a weaker trend is found in the random simulations between steepness and bump strength. Nevertheless, we will show in the next section that the mild correlation found here is statistically smaller than the one obtained for the actual sample. The results of these simulations allow us to assess the limit of applicability of the models. We emphasize that, at present, this is the best possible data to probe the NUV and optical dust extinction law in the Milky Way, with a sample comprising over 10 thousand stars.

4 RESULTS AND DISCUSSION

Fig. 8 shows the trends between the best-fitting effective temperature and some of the parameters that define the sample, from bottom to top, extinction in the V band, distance, and Galactic latitude. The shaded regions encompass a running median along with its (1σ) uncertainty, using a moving interval that includes 200 stars in each trial. In this plot, as well as in the next few figures that apply a similar running median to show the trends of the various parameters, please note that the range on the vertical axis strongly depends on the choice of the horizontal axis, so that it should not come as a surprise that these plots may extend over different ranges, being always smaller than those of the original parameter search of Table 1. Regarding this plot, $T_{\rm eff}$ is derived exclusively from the observed colours (we do not use the absolute fluxes) therefore the trends found with distance and latitude are non-trivial and strengthen the validity of our approach, as we find a strong correlation towards higher temperature stars with increasing distance (as expected in a flux limited survey) and decreasing latitude, as expected from the well-known distribution of stars on the Galactic plane (e.g. Sparke & Gallagher 2007). The blue/red shaded regions in this figure show the split with respect to

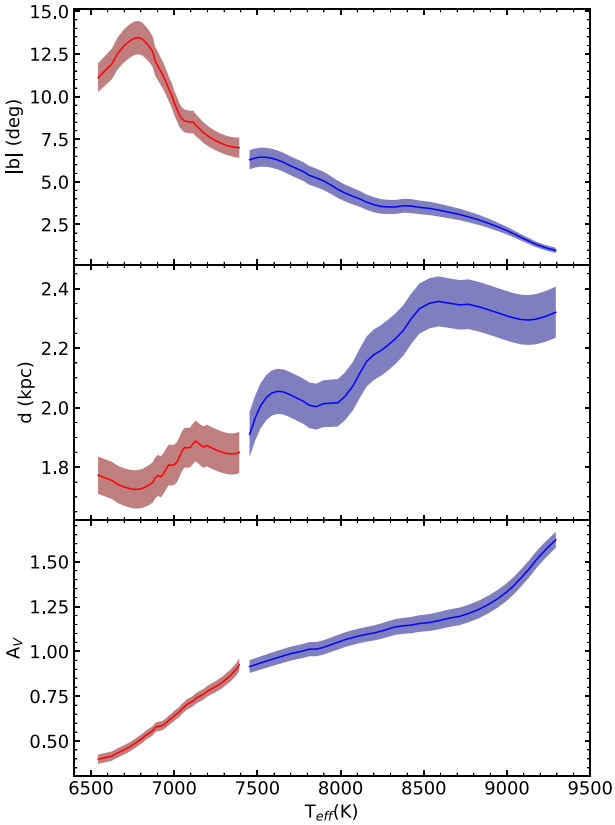

Figure 8. The best-fitting effective temperature is compared with (from top to bottom) Galactic latitude, distance, and V-band extinction. The shaded regions follow a running median along with its uncertainty, binning 200 stars in each trial. The two colours represent the split at the median $T_{\rm eff} = 7500$ K, following the same notation as in Figs 9 and 11.

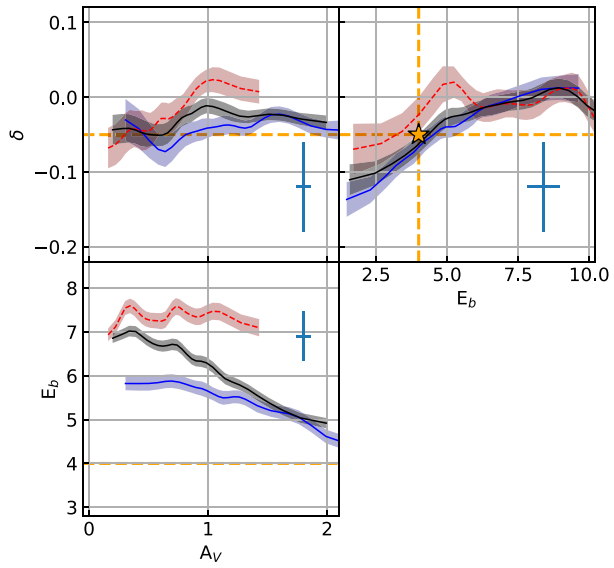

Figure 9. The best-fitting dust extinction parameters are compared among one another. In each panel, the lines represent a running median with respect to the parameter shown in the abscissa, with the shaded region encompassing the 1σ error on the median. Red and blue correspond to subsamples split with respect to effective temperature, split at the median (7500 K) into a hot (blue) and cold (red) subsample. The full sample is shown in grey. The orange lines mark the dust extinction of the standard Milky Way law. The median of the distribution of parameter uncertainties shown in each panel as error bars.

effective temperature at the median value (7500 K), as presented in Figs 9 and 11 below.

The general comparison between the different parameters can be found in Fig. 9, where the three extinction parameters are plotted against each other. We follow the same split with respect to temperature as in Fig. 8. For reference, the orange star and dashed lines mark the Milky Way standard extinction law ($E_b = 4$, $\delta = -0.05$), and a characteristic error bar of the dust parameters is also shown in each panel, defined as the median error bar for each parameter from the MCMC-based fits to the whole sample, given at the 1σ level. Regarding the E_b parameter we note two main results: (i) There is a negative correlation between the NUV bump strength and V-band extinction, mostly caused by the hotter subsample that follows more closely the Galactic plane. The bump is stronger in the cooler subsample. However, this difference might be partly caused by the fact that at lower temperature, the stellar flux is rather weak in the NUV part of the spectrum, and the bump is harder to constrain (see Fig. 6), hence we put more emphasis on the result for the hotter stars. (ii)There is also a slightly positive correlation between δ and E_b, so that steeper laws (i.e. lower values of δ) display weaker bumps. This correlation is independent of the effective temperature. However, the trend is rather mild; note the small variation of the running median for δ. These two results can be put in context with the equivalent relations found in galaxies – i.e. regarding the attenuation law, and thus more complex to disentangle (Kriek & Conroy 2013; Hagen et al. 2017; Tress, et al. 2018; Salim, Boquien & Lee 2018; Decleir et al. 2019). The attenuation studies also find a similar trend towards decreasing E_b with A_V, but the correlation between E_b and δ is opposite to the one found here – although the observational trends show a rather large scatter. We emphasize that the trends with respect to attenuation also depend on dust geometry, and, indeed, some numerical simulations can explain the observed trends with models at constant composition but variable dust geometry (Narayanan et al. 2018). These trends so far have only been reported in dust attenuation studies in galaxies, not in the original extinction curve. Our results suggest that substantial variations in dust composition are present within the same galaxy (in a relatively small volume, $d \lesssim 3$ kpc), so that these variations should be accounted for in any theoretical model of attenuation. This result suggests the carrier responsible for the NUV bump suffers significant variations across different lines of sight, with a well-defined trend towards stronger bumps at low extinction and in regions where the law is shallower. On a speculative tone, one could argue that low extinction regions provide an environment where the formation of large grains is less efficient (i.e. steeper wavelength dependence, and thus, lower δ), whereas in this environment the much smaller carriers of the NUV bump are not destroyed therefore leading to higher E_b. At high values of A_V, the formation of larger grains and a higher efficiency in the destruction of, e.g. PAHs, would lead to the observed relations (Fischera & Dopita 2011). However, it is beyond the scope of this paper to provide a physical scenario to explain these trends.

The validity of these trends can also be quantified by comparing the Pearson correlation coefficient of the data to those quoted above for the best fits corresponding to mock simulations, whose parameters were, by construction, uncorrelated. The results are shown in Table 2, with column 4 showing the correlation coefficients for the actual sample, to be contrasted with column 3 that corresponds to a fully uncorrelated set of mock observations with the same number of stars and with the same flux uncertainties (see Section 3.1). The strong positive correlation between A_V and $T_{\rm eff}$ is confirmed, along with an

anticorrelation between NUV bump strength and A_V. Fig. 9 shows that the cooler subsample features a slight correlation between δ and A_V, and there is also a slightly positive correlation between δ and E_b, so that steeper laws (i.e. lower values of δ) display weaker bumps.

Notice the trend between the steepness parameter (δ) and A_V, with an overall value very close to the commonly adopted Milky Way standard ($\delta = -0.05$, corresponding to $R_V = 3.1$). The cooler subsample features increasing δ with extinction. A simple interpretation of changes in δ would be due to variations in the distribution of dust grain sizes, with smaller grains producing steeper laws (i.e. tending to Rayleigh scattering) and larger grains tending towards a weak wavelength dependence (i.e. tending to Mie scattering). Our results suggest that the general distribution of dust particle sizes does not depend strongly on the net amount of dust extinction, with a weak correlation towards greyer extinction with increasing A_V (expected in dust with a higher contribution from larger grains). Note that the attenuation law in galaxies also becomes shallower at increasing amounts of dust (see e.g. Chevallard et al. 2013; Hagen et al. 2017; Salim et al. 2018; Tress et al. 2018; Decleir et al. 2019), an effect expected from the inhomogeneous distribution of dust within the stellar populations of a galaxy (e.g. Witt & Gordon 2000).

Fig. 10 shows the spatial distribution of the dust extinction parameters, from top to bottom: A_V, E_b, and δ. The Aitoff projections are shown in Galactic coordinates. We should emphasize that our working sample originates from all available pointings made by the *Swift*/UVOT instrument, assembled in the Serendipitous Source Catalogue. Therefore, it is not a dedicated/programmed survey, and only consists of what could be considered sets of random pointings on the sky. This means that the sky is covered very sparsely, with many sources located within relatively narrow patches – the field of view of UVOT is 17×17 arcmin^2 (Roming et al. 2005). Therefore, to create a meaningful representation of the spatial variations of the dust parameters, we grouped all source detections within a single UVOT pointing and obtained single measurements of (A_V, E_b, δ) that correspond to the median of the dust fits within the same field of view. Within each group, we found that the scatter of the dust parameters is roughly compatible with the expected uncertainties. For instance, the scatter of the intra-group parameters – i.e. the distribution of measurements of A_V, E_b, δ towards stars within the same field of view of the UVOT camera – has a median of $\sigma(A_V) = 0.15$, $\sigma(E_b) = 1.7$, $\sigma(\delta) = 0.15$.

The figure shows that most of our targets are located on a thin layer of the Galactic plane – we emphasize that this sample is constrained to have all NUV fluxes with uncertainty below 20 per cent therefore restricting the sample to hotter, more luminous stars, mostly around the turn-off point of the main sequence (see Fig. 3). The top panel illustrates the expected increase in total extinction towards the plane of the Galaxy, more clearly shown in Fig. 11. The middle panel shows a random distribution of NUV bump strengths. The bottom panel shows some weak coherence in the variation of the steepness parameter, δ, not only in latitude but also in longitude, with a preference for lower values of δ towards $\ell \sim$30–120 degrees.

A more detailed view of these trends can be seen in Fig. 11 where we show the projection of the dust extinction parameters (vertical axes) along the three astrometric quantities (from left to right: distance, Galactic latitude, and longitude), following the same running median criteria as in Fig. 9. In the top row it is worth highlighting the strong increasing extinction towards low Galactic latitude, with values $A_V \gtrsim 1$ close to the Galactic plane ($|b| < 10^\circ$). Note that this correlation confirms the validity of the parameter constraints, as it is derived from totally independent methods (i.e. astrometry versus flux ratios). Moreover the strong anticorrelation

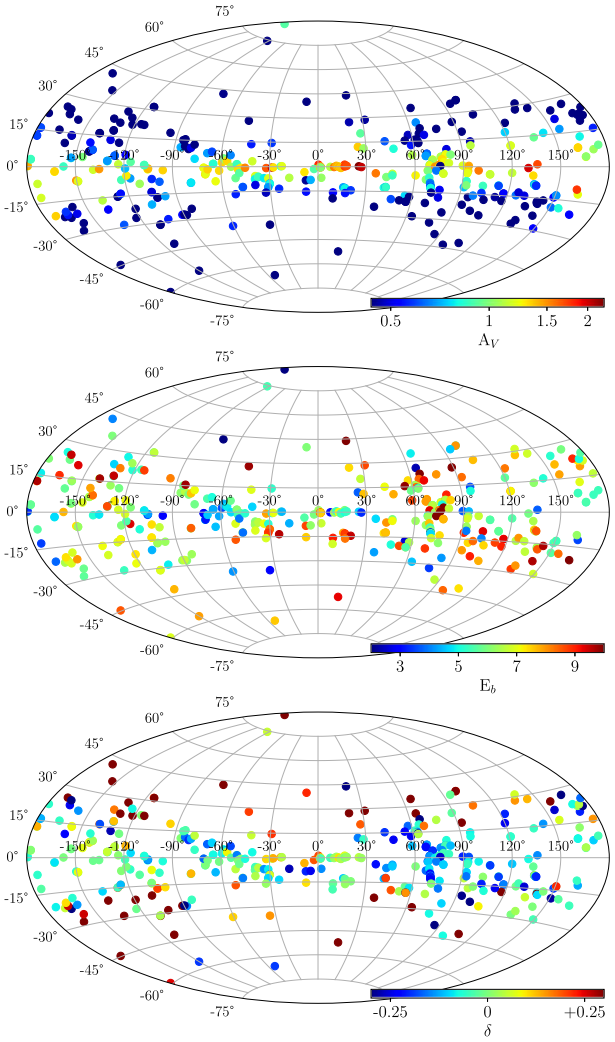

Figure 10. Aitoff projections of our working sample, colour coded with respect to the three extinction parameters, from top to bottom: *V*-band extinction (A_V), NUV bump strength (E_b), and steepness of the wavelength dependence (δ). Note that the sample of 10 452 stars originates from the UVOT Serendipitous Source Catalogue, that is not designed to map the whole sky. Therefore, the coverage is sparse, and the whole set is reduced to pointings within the same field of view of the UVOT camera. The colour-coded dots follow average values within each pointing.

between A_V and $|b|$ is found regardless of temperature, although the cooler subsample extends to higher latitude, as shown in Fig. 8. The trend between A_V and distance depends on temperature: at fixed distance, the hotter subsample features higher extinction, a result due in part to the previous correlation, and the fact that hotter stars are preferentially found at lower Galactic latitude (Fig. 8). However, a selection bias might be present, as the cooler stars at high extinction will not be included in this NUV flux-limits sample. The NUV bump strength (middle panels) is highly covariant with distance, with the sightlines towards the more distant stars showing the weaker bump strengths. Noting the trend between A_V and E_b shown in Fig. 9 along with the mild increase of A_V with distance, we could argue that the nearer stars probe regions of lower extinction, where the bump is expected to be stronger. The strong separation with respect to effective temperature is, once more, apparent, as in Fig. 9. Finally, in the bottom panels we show δ, that appears mostly correlated with latitude, with steeper laws towards the Galactic plane. The previously

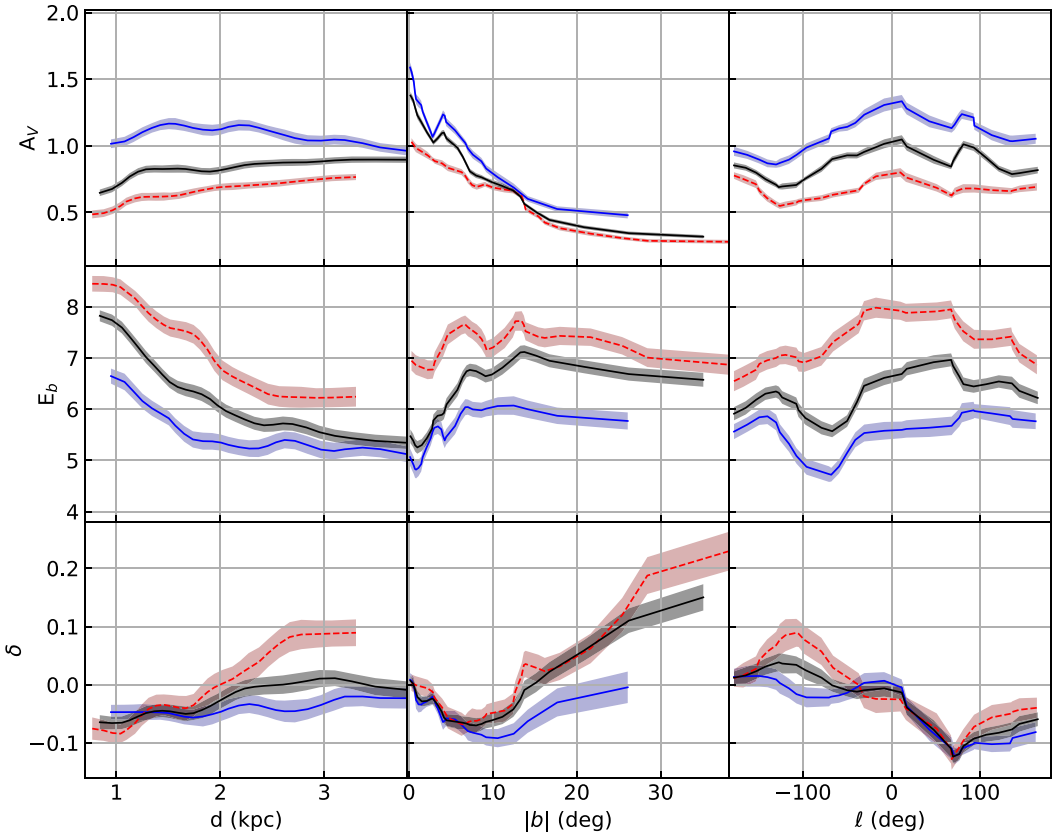

Figure 11. Equivalent of Fig. 9 for the distribution of the dust extinction parameters (ordinate, from top to bottom: *V*-band extinction, NUV bump strength, and steepness of the wavelength dependence) with respect to astrometric quantities (abscissa, from left to right: distance, Galactic latitude, and longitude). The plots show a running median for the whole sample (grey) and split with respect to temperature into hotter (blue) and cooler (red) stars, split at $T_{\rm eff} = 7500$ K.

mentioned 'dip' at $\ell \sim$30–120 degrees is also evident here. It is also worth mentioning that the cooler stars drive the trends of δ, possibly due to the fact that these stars are more spread in Galactic latitude, hence probing more diverse regions regarding dust composition. This result would naively suggest that at lower Galactic latitude, large dust grains are destroyed more efficiently, leading to a steeper extinction law. Note, though, that the behaviour of E_b suggests no significant variation with Galactic latitude in the cooler subset, and that A_V *decreases* quite strongly with latitude. The interpretation of these trends is non-trivial given the interlinked dependence between A_V, steepness and bump strength, requiring a detailed analysis based on a dust model along with a proper radiative transfer treatment in a disc-like geometry, beyond the scope of this paper. We also note that no significant trends have been found in the other panels.

5 SUMMARY

By cross-matching the *Swift*/UVOT Serendipitous Source Catalogue (Yershov et al. 2014) with Data Release 2 of the *Gaia* mission (Gaia Collaboration 2018) and the *2MASS* point source catalogue (Cutri et al. 2003), we assembled a sample of 10 452 stars with good photometry covering a wide spectral range from the near ultraviolet (with filters that straddle the well-known dust absorption feature at 2175 Å) to near-infrared. The sample extends out to several kpc (95 per cent of the sample is located within 3.7 kpc), and is limited in effective temperature ($T_{\rm eff} > 6500$ K) in order to have enough flux in the NUV to constrain the NUV bump. A comparison of the colours with a grid of synthetic stellar atmospheres from the models of Coelho (2014) allows us to constrain the most fundamental parameters of dust extinction in this spectral window, namely the steepness of the wavelength dependence (δ), the strength of the NUV bump (E_b), and the *V*-band extinction (A_V), following the standard prescription of Noll et al. (2009). We note that the serendipitous nature of this data set produces sparse sampling on the sky, preventing us from producing a dust map (e.g. Chen et al. 2019; Lallement et al. 2019). However, this is the first time a large sample (comprising over 10 thousand stars) is used to constrain *both* optical and NUV features of the dust extinction law of the Galaxy.

In addition to the well-known correlation between total extinction and Galactic latitude (Fig. 11), we find in Fig. 9 that the NUV bump strength appears anticorrelated with total extinction (A_V) and positively correlated with the extinction law steepness (δ). Comparisons with simulations allow us to reject the hypothesis of a systematic from the inherent degeneracies as the cause of these trends (Table 2). These trends are stronger in the subsample of hotter stars – mostly located towards low Galactic latitude. The steepness of the extinction law does not vary significantly when plotted with respect to A_V, and appears consistent with the value adopted for the Milky Way standard ($\delta = -0.05$).

In Fig. 10, we show the distribution of our sample in Galactic coordinates, colour coded according to the dust extinction parameters. We note the sparsity of the set, as the parent sample originates from the analysis of all sources found in archival images of the *Swift*/UVOT camera, and therefore does not follow an optimal survey strategy. Despite the low coverage of the sky, the strong trend between A_V and Galactic latitude is apparent once more. The steepness of

the extinction law also appears to be correlated with latitude, and perhaps longitude, with a prominence of low δ (i.e. steeper law) around $\ell \sim 30$–120°. A more detailed illustration of the trends with astrometric quantities is shown in Fig. 11. This paper presents for the first time substantial correlations between dust extinction parameters, analogous but not equivalent to such variations in the dust *attenuation* law in galaxies. A more detailed analysis comprising large samples of spectroscopic data including the NUV optical window (e.g. Gordon et al. 2009; Fitzpatrick et al. 2019) is needed to confirm or refute the trends presented here. Understanding in detail the extinction law in the Galaxy is a very important stage in the more general area of galaxy formation and evolution. Dust attenuation in galaxies remains an open problem, where dust composition and its distribution among the stellar populations play equally important roles (see e.g. Galliano et al. 2018, and references therein). Therefore, constraints on dust extinction parameters derived from nearby resolved systems allow us to understand one of these important components. Our results emphasize that theoretical/numerical models of galaxy formation have to take into account dust composition variations to explain the observed trends in the dust attenuation law, as simple models based on a fixed composition would not be able to explain these trends in our own Galaxy.

ACKNOWLEDGEMENTS

The referee is warmly thanked for a very careful reading of this paper, providing useful comments and suggestions that have improved this paper. This work has made use of data from the European Space Agency (ESA) mission *Gaia* (http://www.cosmos.esa.int/gaia), processed by the *Gaia* Data Processing and Analysis Consortium (DPAC, http://www.cosmos.esa.int/web/gaia/dpac/consortium). Funding for the DPAC has been provided by national institutions, in particular the institutions participating in the *Gaia* Multilateral Agreement. This research made use of the cross-match service provided by CDS, Strasbourg. MP was supported by the UK Science and Technology Facility Council (STFC), grant number ST/N000811/1. MP and PK acknowledge support from the UK Space Agency. The authors acknowledge the use of the UCL Myriad High Throughput Computing Facility (Myriad@UCL), and associated support services, in the completion of this work.

DATA AVAILABILITY

This sample is extracted from a cross-match of publicly available data sets (UVOT Serendipitous Source Catalogue, *Gaia* DR2, and *2MASS* point source catalogue). The combined final data set is available upon request.

REFERENCES

Alzate J. A., Bruzual G., Díaz-González D. J., 2021, MNRAS, 501, 302
Bai Y., Liu J., Bai Z., Wang S., Fan D., 2019, AJ, 158, 93
Bailer-Jones C. A. L., Rybizki J., Fouesneau M., Mantelet G., Andrae R., 2018, AJ, 156, 58
Bradley J. et al., 2005, Science, 307, 244
Bressan A., Marigo P., Girardi L., Salasnich B., Dal Cero C., Rubele S., Nanni A., 2012, MNRAS, 427, 127
Calzetti D., Armus L., Bohlin R. C., Kinney A. L., Koornneef J., Storchi-Bergmann T., 2000, ApJ, 533, 682
Cardelli J. A., Clayton G. C., Mathis J. S., 1989, ApJ, 345, 245
Chen B.-Q. et al., 2019, MNRAS, 483, 4277
Chevallard J., Charlot S., Wandelt B., Wild V., 2013, MNRAS, 432, 2061
Coelho P. R. T., 2014, MNRAS, 440, 1027
Coelho P. R. T., Bruzual G., Charlot S., 2020, MNRAS, 491, 2025
Conroy C., Schiminovich D., Blanton M. R., 2010, ApJ, 718, 184
Cutri R. M. et al., 2003, yCat, II/246
Decleir M. et al., 2019, MNRAS, 486, 743
Draine B. T., 2003, ARA&A, 41, 241
Duley W. W., Seahra S., 1998, ApJ, 507, 874
Fischera J., Dopita M., 2011, A&A, 533, A117
Fitzpatrick E. L., 1999, PASP, 111, 63
Fitzpatrick E. L., Massa D. L., 1990, ApJS, 72, 163
Fitzpatrick E. L., Massa D. L., 2007, ApJ, 663, 320
Fitzpatrick E. L., Massa D., Gordon K. D., Bohlin R., Clayton G. C., 2019, ApJ, 886, 108
Foreman-Mackey D., Hogg D. W., Lang D., Goodman J., 2013, PASP, 125, 306
Gaia Collaboration, 2018, A&A, 616, A1
Galliano F., Galametz M., Jones A. P., 2018, ARA&A, 56, 673
Gordon K. D., Clayton G. C., Misselt K. A., Landolt A. U., Wolff M. J., 2003, ApJ, 594, 279
Gordon K. D., Cartledge S., Clayton G. C., 2009, ApJ, 705, 1320
Gregg M. D. et al., 2006, hstc.conf, 209
Hagen L. M. Z., Siegel M. H., Hoversten E. A., Gronwall C., Immler S., Hagen A., 2017, MNRAS, 466, 4540
Hoversten E. A. et al., 2011, AJ, 141, 205
Hutton S. et al., 2014, MNRAS, 440, 150
Hutton S., Ferreras I., Yershov V., 2015, MNRAS, 452, 1412
Kriek M., Conroy C., 2013, ApJ, 775, L16
Lallement R. et al., 2019, A&A, 625, A135
Narayanan D., Conroy C., Davé R., Johnson B. D., Popping G., 2018, ApJ, 869, 70
Noll S. et al., 2009, A&A, 499, 69
Oke J. B., Gunn J. E., 1983, ApJ, 266, 713
Page M. J. et al., 2014, Proceedings of Scinec (SWIFT-10) Vol. 037, The Swift UVOT Serendipitous Source Catalogue. SISSA, Trieste, PoS(SWIFT 10)037
Panuzzo P., Granato G. L., Buat V., Inoue A. K., Silva L., Iglesias-Páramo J., Bressan A., 2007, MNRAS, 375, 640
Pei Y. C., 1992, ApJ, 395, 130
Roming P. W. A. et al., 2005, SSRv, 120, 95
Salim S., Boquien M., Lee J. C., 2018, ApJ, 859, 11
Sparke L. S., Gallagher J. S., 2007, Galaxies in the Universe. Cambridge Univ. Press, Cambridge UK,
Tress M. et al., 2018, MNRAS, 475, 2363
Tress M. et al., 2019, MNRAS, 488, 2301
Valencic L. A., Clayton G. C., Gordon K. D., 2004, ApJ, 616, 912
Weingartner J. C., Draine B. T., 2001, ApJ, 548, 296
Witt A. N., Gordon K. D., 2000, ApJ, 528, 799
Yershov V. et al., 2014, Ap&SS, 354, 97

This paper has been typeset from a TEX/LATEX file prepared by the author.